PHYSICAL REVIEW MATERIALS **6**, 074001 (2022)

Atomic ordering and phase separation in lateral heterostructures and multijunctions of ternary two-dimensional hexagonal materials

Zhi-Feng Huang
Department of Physics and Astronomy, Wayne State University, Detroit, Michigan 48201, USA

(Received 26 April 2022; accepted 22 June 2022; published 5 July 2022)

The growth and microstructural properties of ternary monolayers of two-dimensional hexagonal materials are examined, including both individual two-dimensional crystalline grains and in-plane heterostructures, multijunctions, or superlattices. The study is conducted through the development of a ternary phase field crystal model incorporating sublattice ordering and the coupling among the three atomic components. The results demonstrate that a transition of compositional pattern or modulation in this type of two-dimensional ternary crystals, from phase separation to geometrically frustrated lattice atomic ordering, can be controlled via the varying degree of energetic preference of heteroelemental neighboring over the homoelemental ones. Effects of growth and system conditions are quantitatively identified through numerical calculations and analyses of interspecies spatial correlations and the degree of alloy intermixing or disordering. These findings are applied to simulating the growth of monolayer lateral heterostructures with atomically sharp heterointerface, and via the sequential process of edge epitaxy, the formation of the corresponding superlattices or structures with multiple heterojunctions, with outcomes consistent with recent experiments of in-plane multiheterostructures of transition-metal dichalcogenides. Also explored is a distinct type of alloy-based lateral heterostructures and multijunctions, which integrate ternary ordered alloy domains with the adjoining blocks of binary compounds, providing a more extensive variety of two-dimensional heterostructural materials.

DOI: 10.1103/PhysRevMaterials.6.074001

I. INTRODUCTION

While the two-dimensional (2D) edge-epitaxial growth of in-plane lateral heterostructures has been achieved recently, including the fabrication of heterojunctions connecting different types of monolayer blocks of transition-metal dichalcogenides (TMDs) [1–8] or between graphene and hexagonal boron nitride (*h*-BN) [9], and the *in situ* synthesis of various TMD lateral multijunctions or superlattices [10–14], their further development is hindered by the difficulties related to the controllability of the growth process and heterointerfacial properties. The major challenges in controlling the growth and property of these heterostructures involve various coupled factors, such as the structural control at the atomic level, concerning the sharpness of heterointerfaces and defect formation, and the compositional control with effects of intermixing or alloying of different atomic components either at interface or in bulk. They are key to determining the functionality of heterostructures and their device applications, and to enabling the engineering of electronic band structures, thermal transport, or magnetic property, with examples including the fabrication of TMD-based p-n junctions [1–4] or metal-semiconductor heterojunctions [7], metal-insulator (e.g., graphene-*h*-BN) lateral tunneling structures [9], and atomically thin in-plane quantum wells and quasi-1D superlattices [10–12].

Another key factor involved, which is intrinsic to multicomponent material systems, is related to the behavior of mixing vs demixing between different atomic species, yielding the phenomenon of short-range lattice atomic ordering vs phase separation. For an AB/CB-type heterostructure, such as TMD/TMD heterostructure in the form of $MX_2/M'X_2$ or MX_2/MX'_2 with M, M' a transition-metal element (e.g., Mo, W, Nb, Re) and X, X' a chalcogen element (e.g., S, Se, Te), phase separation between domains of AB and CB compounds seemingly occurs. However, the 2D bulk state of $A_xC_{1-x}B_2$ ternary TMD alloys, such as $\mathrm{Mo}_{1-x}\mathrm{W}_x X_2$ [15,16] and $\mathrm{Re}_{0.5}\mathrm{Nb}_{0.5}\mathrm{S}_2$ [17], does not reveal any phase-separated behavior; instead, either random alloying or atomic ordering between A and C components (which could form a triangular lattice with geometric frustration [17]) has been found. This can be attributed to the energetic competition or preference between heteroelemental (A-C) and homoelemental (A-A and C-C) interactions, which in 2D TMD alloys gives the energy gain for forming A-C heteroatomic neighboring [15] as a result of charge transfer between different species [16]. Thus, to synthesize a lateral heterostructure or multijunction separating AB and CB phases via, e.g., chemical or physical vapor deposition, instead of a 2D bulk growth of ternary mixture, experimentally a sequential process of edge epitaxy through the control of deposition flux is used, with the next block of new material (e.g., CB) grown epitaxially from the edge of the as-grown domain of a different material (e.g., AB). Repeating this sequence leads to the formation of in-plane multijunctions or superlattices with alternating domains or blocks of different 2D materials [10–12].

The above structural and compositional properties of 2D materials can be varied through the control of sample growth conditions, with a typical one being the growth temperature. For the bulk state of ternary TMD alloys, high enough temperature would result in the disordering and random alloying of the monolayer material such as $\mathrm{Mo}_{1-x}\mathrm{W}_x\mathrm{S}_2$ [15,18]. Variation of growth temperature also affects the interfacial sharpness of heterostructural systems. Enhanced diffusion at higher temperature (and low growth rates) leads to more compositionally intermixed and diffuse or roughening interfaces with substitutional alloying, while at low temperatures (and/or fast deposition rates with limited edge-diffusion process) narrow or atomically sharp heterointerfaces are generated, as observed in experiments of in-plane TMD/TMD heterojunctions [1,3,6,13].

Although both experimental and theoretical efforts have been devoted to examining those various factors described above, the understanding of them is still far from complete due to the complexity of the dynamical growth process of heterostructures and the large spatial and temporal scales involved. Most of the related theoretical analyses and modeling are based on small-system atomistic calculations [including first-principles calculations and molecular dynamics (MD) or Monte Carlo simulations] with limited time and length scales, while a systematic understanding is still lacking. What is also lacking, in both experimental and theoretical or computational works, is how to incorporate the effect of atomic ordering of ternary 2D materials into heterostructures or multijunctions, which is expected to induce more tunable functional property of the heterostructural system particularly given the change of electronic property as a result of atomic ordering in each individual domain of ternary 2D alloy [17]. The corresponding growth process will be explored in this work through the development of a phase field crystal (PFC) model for describing the structure and dynamics of in-plane AB/CB type ternary hexagonal materials.

The ternary density-field model introduced here is based on the PFC approach, which is able to resolve microscopic crystalline details of the material system and simulate dynamical processes at large diffusive timescales [19–23]. This method has been used in a wide range of applications such as the study of binary and multicomponent alloy systems [24–27] and 2D hexagonal materials [28–36]. The ternary PFC model developed in this work is for modeling the mixture or alloying of AB- and CB-type 2D material compounds, and is applied to examining the properties of 2D monolayers subjected to vertical confinement when deposited on a substrate (as in the epitaxial growth of real materials). These include the control of phase separation vs atomic ordering in a 2D ternary grain, the characterization of spatial correlation and composition intermixing or disordering under different system conditions, and the formation of laterally edge-epitaxial AB/CB heterostructures and multijunctions consisting of alternating AB and CB blocks with heterointerfaces along the zigzag crystalline direction, which are consistent with recent experimental findings of $\mathrm{Mo}X_2/\mathrm{W}X_2$ (X = S, Se) and $M\mathrm{S}_2/M\mathrm{Se}_2$ (M = Mo, W) 2D heterostructural materials synthesized via multistep, sequential epitaxial growth. The extension to incorporate atomically ordered ACB-type ternary alloy blocks into an interesting new kind of alloy-based in-plane multiheterostructures is predicted, as demonstrated in our PFC simulations generating lateral heterojunctions comprising adjacent blocks of 2D binary compounds and ternary ordered alloys.

II. MODEL

The PFC model for binary AB sublattice ordering can be developed from classical dynamical density functional theory (DDFT) [30,31], where the model system is described by the evolution of atomic density variation fields n_η ($\eta = A, B$) for A and B components, i.e.,

$$\frac{\partial n_\eta}{\partial t} = m_\eta \nabla^2 \frac{\delta \mathcal{F}}{\delta n_\eta}. \tag{1}$$

Here $m_A = 1$ after rescaling, $m_B = M_B/M_A$ with M_A and M_B the atomic mobilities of A and B species, and the rescaled PFC free energy functional $\mathcal{F} = \mathcal{F}_A + \mathcal{F}_B + \mathcal{F}_{AB}$, where $\mathcal{F}_{\eta=A,B}$ is the same as that of single-component PFC, i.e.,

$$\mathcal{F}_\eta = \int d\mathbf{r}\left[-\frac{1}{2}\epsilon_\eta n_\eta^2 + \frac{1}{2}\beta_\eta n_\eta\left(\nabla^2 + q_\eta^2\right)^2 n_\eta - \frac{1}{3}g_\eta n_\eta^3 + \frac{1}{4}v_\eta n_\eta^4\right], \tag{2}$$

while the coupling between A and B components is determined by

$$\mathcal{F}_{AB} = \int d\mathbf{r}\left[\alpha_{AB} n_A n_B + \beta_{AB} n_A \left(\nabla^2 + q_{AB}^2\right)^2 n_B + \frac{1}{2}w_{AB} n_A^2 n_B + \frac{1}{2}u_{AB} n_A n_B^2\right]. \tag{3}$$

All the model parameters (ϵ_η, q_η, β_η, g_η, v_η, α_{AB}, β_{AB}, q_{AB}, w_{AB}, u_{AB}) are dimensionless and can be expressed through the expansion components of the Fourier transform of two- and three-point direct correlation functions [31]. In Eq. (3) the first α_{AB} term yields an energy penalty for the overlap of A and B density maxima (atomic sites), while the last two terms are important for stabilizing the vacancy positions (i.e., without either A or B sites and with the overlap of A and B minima). A number of phases of 2D binary ordering plus a homogeneous state are identified in this model and the corresponding phase diagrams have been calculated [30,31], including the coexistence and phase transformation between them. Among them the binary honeycomb phase, with each of its triangular sublattices occupied by A or B component separately, corresponds to the lattice structure of monolayer h-BN or the in-plane projection of trigonal prismatic 2H phase of MX_2 TMDs, while the phase with triangular $A(B)$ and honeycomb $B(A)$ sublattices is the in-plane version of octahedral 1T phase of TMDs.

This PFC model has been used to identify and predict the defect structure, energy, and dynamics of h-BN grain boundaries [30,36], with results consistent with experiments and atomistic calculations (DFT or MD), and to examine graphene/h-BN and h-BN/h-BN heterostructures and bilayers [33,34] as well as thermal transport of h-BN monolayers [35]. It is important to note that the model can also be applied to a wider range of 2D compound materials with binary honeycomb lattice, including the atomically thin MX_2 TMDs of 2H phase (e.g., M = Mo, W, Nb, X = S, Se; MoTe_2, TaS_2)

and transition-metal chalcogenides of 1H phase (e.g., FeSe) [37]. Although in 2H phase a MX_2 monolayer is composed of X-M-X stacking planes, the two X atoms are always paired and thus can be effectively treated as one base unit occupying a honeycomb lattice together with the M atoms, a configuration that is well described by this in-plane PFC model particularly for the monolayer deposited on a substrate during epitaxy (e.g., the out-of-plane corrugations of MoS_2 grown on Au(111) via physical vapor deposition are mostly less than 1 Å [38], and thus play a secondary role and are neglected in our modeling). This can also be seen from the result that the defect core structures of grain boundaries (e.g., 4|8, 4|4, and 8|8 dislocations) found in MoS_2 [39–41] and $MoSe_2$ [42] samples can be identified from this 2D PFC model [30].

Here the above binary model is extended to an in-plane AB/CB or ACB ternary PFC model describing the mixture of AB and CB compounds (each having its own intrinsic AB or CB sublattice ordering) that are confined on a substrate. The corresponding free energy functional is written as

$$\mathcal{F} = \mathcal{F}_A + \mathcal{F}_B + \mathcal{F}_C + \mathcal{F}_{AB} + \mathcal{F}_{CB} + \mathcal{F}_{AC}, \tag{4}$$

where $\mathcal{F}_{\eta=A,B,C}$ is determined by Eq. (2) giving triangular sublattice for each of A, B, and C components in the crystalline state, while $\mathcal{F}_{AB}$ and $\mathcal{F}_{CB}$ follow Eq. (3) (with $A \rightarrow C$ for $\mathcal{F}_{CB}$) to stabilize AB and CB binary honeycomb lattices, respectively. The specific form of $\mathcal{F}_{CB}$ is written as

$$\mathcal{F}_{CB} = \int d\mathbf{r}\Big[\alpha_{CB} n_C n_B + \beta_{CB} n_C \big(\nabla^2 + q_{CB}^2\big)^2 n_B + \frac{1}{2} w_{CB} n_C^2 n_B + \frac{1}{2} u_{CB} n_C n_B^2\Big]. \tag{5}$$

The tendency of A-C mutual exclusion is built into $\mathcal{F}_{AC}$; to leading order we have

$$\mathcal{F}_{AC} = \int d\mathbf{r}\Big[\beta_{AC} n_A \big(\nabla^2 + q_{AC}^2\big)^2 n_C + \frac{1}{2}\mu_{AC} n_A^2 n_C^2 + \frac{1}{2} w_{AC} n_A^2 n_C + \frac{1}{2} u_{AC} n_A n_C^2\Big], \tag{6}$$

where the parameter β_{AC} controls the degree of proximity (or relative affinity) between A and C species, with larger value of β_{AC} (>0) corresponding to more energetic preference of A-C heteroelemental bonding or neighboring as compared to A-A and C-C homoelemental ones. It is noted that the model introduced here is different from the multicomponent PFC model developed in Ref. [33] for the study of graphene/h-BN phase-separated heterostructure, where the couplings between spatially smoothed density fields (with the filtering of n_η to eliminate short lattice-scale variations) were imposed to control the phase separation and structure stability. This extra treatment of density smoothing is not needed here in our modeling of the AB/CB compound system. Instead, a simple high-order coupling term, $\mu_{AC} n_A^2 n_C^2$, is introduced in Eq. (6) to favor the separation of A and C atomic sites (with both n_A and n_C maxima) and also of their vacancy sites (with both n_A and n_C minima). In addition, the term $\alpha_{AC} n_A n_C$ is neglected here (or equivalently, $\alpha_{AC} = 0$). $\alpha_{AC} > 0$ corresponds to the energetic favoring of A-C heteroelemental bonding, an effect that has already been incorporated in the β_{AC} term, while a more negative value of α_{AC} would lead to a higher degree of A-C site overlap, which should be avoided.

This ternary PFC model, including the newly identified A-C coupling terms in Eq. (6), can be derived from DDFT by following the procedure similar to that given in Ref. [31] for binary systems. In addition to those two- and three-point direct correlation functions of classical DFT that are used to identify the PFC terms in Eqs. (2)–(5) for A-B and C-B binary sublattice ordering, the Fourier-space expansions of two-, three-, and four-point direct correlations between A and C components are needed to obtain the new β_{AC}, w_{AC}, u_{AC}, and μ_{AC} terms of A-C coupling in Eq. (6), respectively. In principle, this ternary PFC model can be extended to incorporate out-of-plane deformations of AB/CB or ACB monolayers, by using the approach developed in Ref. [34] with the coupling to the variation of an additional field of vertical surface height. In the epitaxial system examined here, with substrate confinement and hence rather weak vertical variations of the grown overlayers as observed experimentally and described above, out-of-plane deformations would be of secondary or negligible effect and thus are not considered in this study.

The dynamics of three density variation fields n_A, n_B, and n_C are governed by Eq. (1). Substituting Eq. (4), with the use of Eqs. (2), (3), (5), and (6), gives

$$\begin{aligned}\frac{\partial n_A}{\partial t} &= m_A \nabla^2\Big[-\epsilon_A n_A + \beta_A\big(\nabla^2 + q_A^2\big)^2 n_A - g_A n_A^2 \\ &\quad + v_A n_A^3 + \alpha_{AB} n_B + \beta_{AB}\big(\nabla^2 + q_{AB}^2\big)^2 n_B \\ &\quad + w_{AB} n_A n_B + \frac{1}{2} u_{AB} n_B^2 + \beta_{AC}\big(\nabla^2 + q_{AC}^2\big)^2 n_C \\ &\quad + \mu_{AC} n_A n_C^2 + w_{AC} n_A n_C + \frac{1}{2} u_{AC} n_C^2\Big],\end{aligned} \tag{7}$$

$$\begin{aligned}\frac{\partial n_B}{\partial t} &= m_B \nabla^2\Big[-\epsilon_B n_B + \beta_B\big(\nabla^2 + q_B^2\big)^2 n_B - g_B n_B^2 \\ &\quad + v_B n_B^3 + \alpha_{AB} n_A + \beta_{AB}\big(\nabla^2 + q_{AB}^2\big)^2 n_A \\ &\quad + u_{AB} n_A n_B + \frac{1}{2} w_{AB} n_A^2 + \beta_{CB}\big(\nabla^2 + q_{CB}^2\big)^2 n_C \\ &\quad + \alpha_{CB} n_C + u_{CB} n_C n_B + \frac{1}{2} w_{CB} n_C^2\Big],\end{aligned} \tag{8}$$

$$\begin{aligned}\frac{\partial n_C}{\partial t} &= m_C \nabla^2\Big[-\epsilon_C n_C + \beta_C\big(\nabla^2 + q_C^2\big)^2 n_C - g_C n_C^2 \\ &\quad + v_C n_C^3 + \alpha_{CB} n_B + \beta_{CB}\big(\nabla^2 + q_{CB}^2\big)^2 n_B \\ &\quad + w_{CB} n_C n_B + \frac{1}{2} u_{CB} n_B^2 + \beta_{AC}\big(\nabla^2 + q_{AC}^2\big)^2 n_A \\ &\quad + \mu_{AC} n_A^2 n_C + u_{AC} n_A n_C + \frac{1}{2} w_{AC} n_A^2\Big],\end{aligned} \tag{9}$$

which are used in our simulations of 2D ternary AB/CB-type material systems.

III. RESULTS

The PFC dynamical equations (7)–(9) are solved numerically via a pseudospectral method with the imposing of periodic boundary conditions, starting from various initial

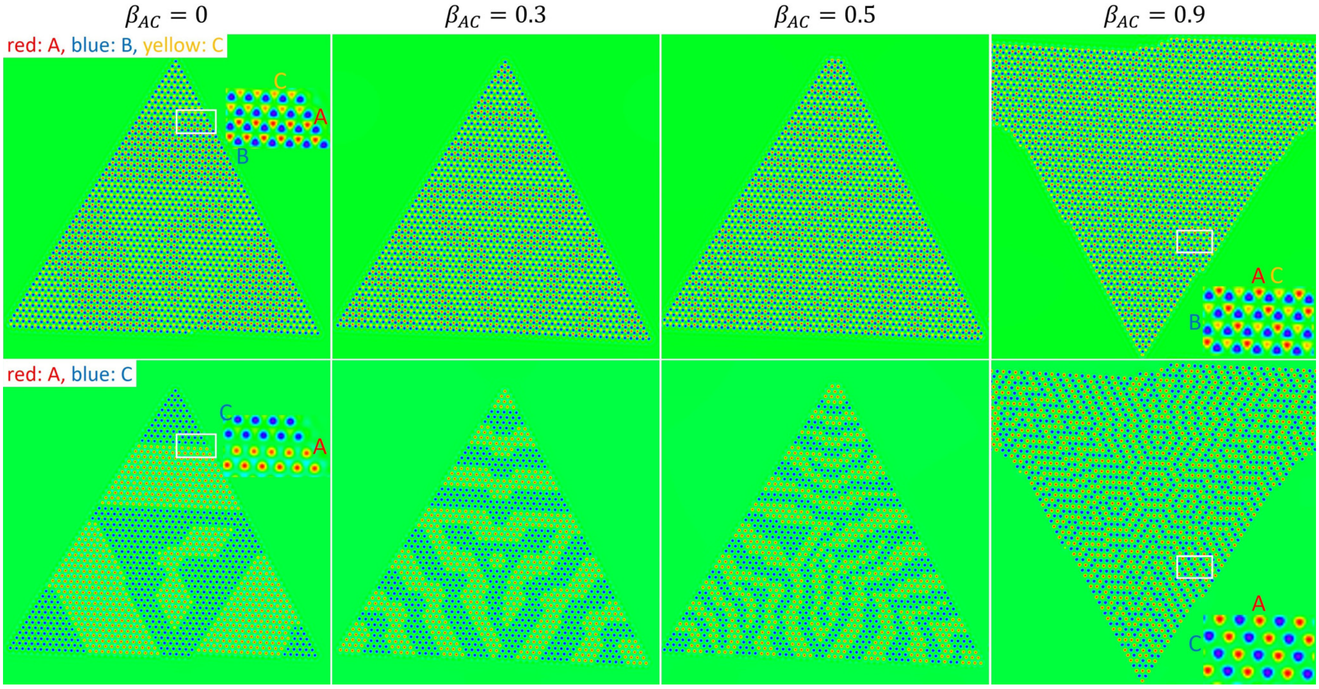

FIG. 1. Sample simulation snapshots of ternary 2D single crystals with hexagonal lattice symmetry surrounded by a homogeneous state, showing a transition from phase separation to atomic ordering between A and C species as the value of β_{AC} increases. Results are generated at $t = 10^4$ for $\epsilon = 0.3$ and average densities $n_{A0} = n_{B0} = n_{C0} = -0.383$, starting from an initial single nucleus with only one A and one B atoms embedded in the homogeneous media. Top panels: Spatial distributions of all three densities n_A, n_B, and n_C. Bottom panels: The corresponding spatial distributions of n_A and n_C only (noting the change of C-site coloring from yellow to blue as compared to the top panels for a better contrast). Some portions of the simulated atomic configurations (white-boxed) are enlarged as insets, showing either phase-separated or atomically ordered lattice structures.

conditions. For simplicity, the in-plane systems studied in this work are free of heterointerfacial defects or morphological modulations, as found in many AB/CB-type experimental systems (e.g., TMD/TMD heterostructures) with small enough lattice mismatch so that the misfit-induced effects can be neglected at least to lowest order. This will enable us to focus here on the properties of phase separation or demixing, atomic ordering, intermixing, and the formation of lateral heterostructures and multijunctions through PFC modeling. Results for more complex scenarios caused by misfit strains, such as the stress-driven structural variations or dislocation formation. which can also be well addressed by this PFC model, will be presented elsewhere. In the following the model parameters are set as $\beta_\eta = 1$, $q_\eta = 1$, $g_\eta = 0.5$, $v_\eta = 1$, and $m_\eta = 1$ (with $\eta = A, B, C$), as well as $\alpha_{AB} = \alpha_{CB} = 0.5$, $\beta_{AB} = \beta_{CB} = 0.02$, $q_{AB} = q_{CB} = q_{AC} = 1$, $\mu_{AC} = 1$, and $w_{AB} = w_{CB} = w_{AC} = u_{AB} = u_{CB} = u_{AC} = 0.3$. Values of parameter β_{AC} characterizing A-C heteroelemental interaction, the effective temperature parameter $\epsilon_A = \epsilon_B = \epsilon_C = \epsilon$, and average densities $n_{\eta 0}$ are varied to represent different growth and sample conditions.

A. Effect of heteroelemental interaction: Atomic ordering versus phase separation

Analogous to the well-known scenarios of phase separation (demixing) vs short-range lattice ordering in binary alloying systems, it is expected that the 2D AB/CB ternary materials studied here, with sublattice-ordered structure in each of the AB and CB compounds, would reveal a similar behavior giving either the separation between AB and CB honeycomb phases or an atomically ordered phase with an additional lattice ordering between A and C components. This effect has been built into our PFC model via the β_{AC} term in Eq. (6) representing the degree of energetic preference of A-C heteroelemental bonding over A-A and C-C homoatomic interactions, and is shown explicitly in our simulation results illustrated in Fig. 1. Here the nucleated growth of 2D ternary crystallites is simulated, as initiated from a single nucleus and surrounded by a homogeneous phase of A, B, and C densities with $n_{A0} = n_{B0} = n_{C0} = -0.383$ at $\epsilon = 0.3$. Inside a 2D crystal sheet of triangle shape (as found in most experiments of TMD monolayers grown epitaxially), the phase-separated state with unmixing AB and CB domains occurs at small enough β_{AC}, while the average size or length scale of the stripelike domain pattern reduces with the increase of β_{AC}. At large enough value of β_{AC}, i.e., large enough energetic preference for heteroatomic coordination, a transition to the A-C atomic ordering occurs, showing as a fully ordered lattice structure with A and C components forming a triangular lattice while each of AB and CB still maintaining its binary honeycomb atomic configuration [see both the A-B-C (top panel) and A-C (bottom panel) density distributions in the insets of Fig. 1 for $\beta_{AC} = 0.9$]. This is of the same atomically ordered structure observed in the recent experiment of 2D $\mathrm{Re_{0.5}Nb_{0.5}S_2}$ TMD alloy, resembling a geometrically frustrated system with Re(A)-Nb(C) triangular lattice [17].

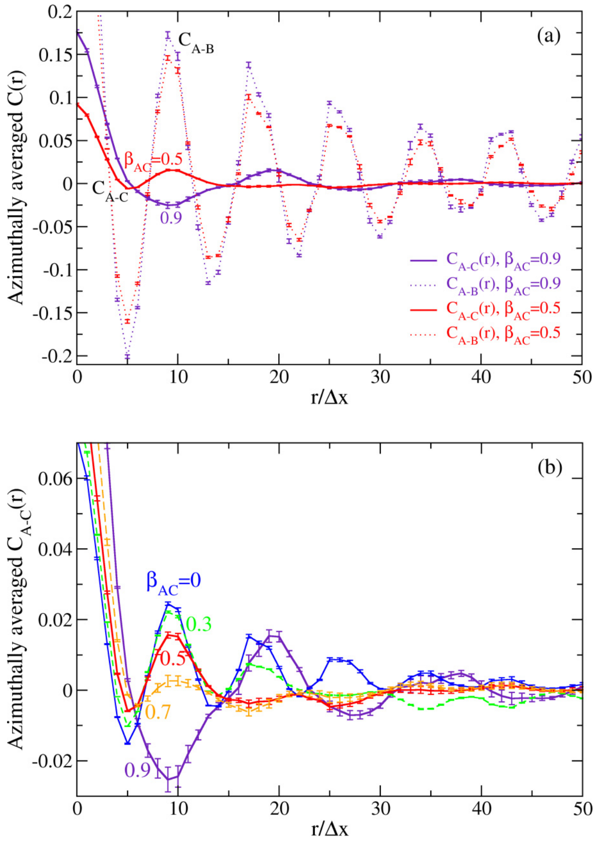

FIG. 2. Azimuthally averaged correlation functions for different values of β_{AC} at $\epsilon = 0.3$ and $n_{A0} = n_{B0} = n_{C0} = -0.383$. (a) Correlation functions $C_{\text{A-C}}(r)$ and $C_{\text{A-B}}(r)$ for $\beta_{AC} = 0.5$ and 0.9. (b) Results of $C_{\text{A-C}}(r)$ for $\beta_{AC} = 0$, 0.3, 0.5, 0.7, and 0.9 [note the much smaller scale of the vertical axis as compared to (a)]. Some of the corresponding atomic structures are given in Fig. 1. The data has been averaged over 20 simulations per each value of β_{AC}.

The property of lattice ordering can be quantified via the equal-time pair correlation function

$$\begin{aligned} C_{\eta\text{-}\eta'}(\mathbf{r}, t) &= \langle [n_\eta(\mathbf{x}+\mathbf{r}, t) - n_{\eta'}(\mathbf{x}+\mathbf{r}, t)][n_\eta(\mathbf{x}, t) - n_{\eta'}(\mathbf{x}, t)]\rangle \\ &\quad - \langle n_\eta - n_{\eta'}\rangle^2, \end{aligned} \tag{10}$$

where $\eta \neq \eta'$ and $\eta, \eta' = A, B, C$. In the crystalline state the density fields n_η and $n_{\eta'}$ vary periodically in space, and a positive maximum of spatial correlation $C_{\eta\text{-}\eta'}$ at a displacement $\mathbf{r}$ indicates a homoelemental η-η or η'-η' pair of atomic sites with separation of $\mathbf{r}$, while a negative minimum of $C_{\eta\text{-}\eta'}$ corresponds to a heteroelemental η-η' atomic pair instead. Some results of the azimuthal average of $C_{\eta\text{-}\eta'}$, including $C_{\text{A-C}}(r)$ and $C_{\text{A-B}}(r)$ at time $t = 10^4$ (each averaged over 20 independent simulation runs initialized with different random number seeds for the homogeneous media), are given in Fig. 2. As expected, the first negative minimum of the oscillatory $C_{\text{A-B}}(r)$ shown in Fig. 2(a) is located at $r = a_{AB} \sim 5\Delta x$ (with the simulation grid spacing $\Delta x = \pi/4$), which is the distance of A-B nearest neighboring in an AB honeycomb unit ring, and the next positive maximum of $C_{\text{A-B}}(r)$ appears at $r = a_0 \simeq \sqrt{3}a_{AB}$ corresponding to either A-A or B-B neighboring, i.e., the lattice spacing of binary AB honeycomb structure. Similar results for the CB honeycomb lattice ordering can be obtained from the correlation $C_{\text{C-B}}$.

Quantitative information for the A-C segregation or ordering can be extracted from the correlation function $C_{\text{A-C}}(r)$. As seen in Fig. 2(b), large enough value of β_{AC} (e.g., $= 0.9$) leads to a negative minimum of $C_{\text{A-C}}$ at $r = a_0$, which corresponds to the nearest-neighbor spacing of A-C-A or C-A-C triangular lattice with more A-C heteroatomic neighboring that results in the negative value of spatial correlation. This agrees with the result of Re-Nb spatial correlation in $\text{Re}_{0.5}\text{Nb}_{0.5}\text{S}_2$ monolayer measured in Ref. [17]. The next positive maximum of correlation is found at $r \simeq 2a_0$, which can be attributed to the homoatomic next-nearest neighbor (A-A or C-C) of the binary AC lattice. These then indicate the A-C atomic ordering with $ACAC\ldots$ alternative lines of atoms as shown in the bottom-right inset of Fig. 1. On the other hand, Fig. 2(b) also shows that at smaller β_{AC} (e.g., $0 \leqslant \beta_{AC} \leqslant 0.7$) a positive maximum of $C_{\text{A-C}}$ instead occurs at $r = a_0$, indicating the dominance of homoelemental A-A or C-C lattice inside each phase-segregated domain. The height of this maximum peak decreases with the increase of β_{AC}, due to the contribution of negative correlation from larger portion of A-C heterointerfaces separating domains of smaller size. This domain size reduction is corroborated by the less number of correlation peaks located at larger distances r and also shorter range of positive spatial correlation (or faster decay of the envelop of positive correlation peaks) when β_{AC} becomes larger. All these results are consistent with the simulation outcomes presented in Fig. 1 for a transition between states of phase separation and short-range atomic ordering.

B. Intermixing and disordering

During the growth and evolution of 2D ternary TMD monolayers, the compositional intermixing or disordering of AB vs CB compound has been observed, showing as the random distribution or alloying of A or C components in the experimental samples (e.g., $\text{Mo}_{1-x}\text{W}_x\text{S}_2$ [6,18]). In our PFC modeling this behavior is represented by the degree of intermixing between A and C species (or the probability of A-C intermixing). This can be identified quantitatively via the following two factors. The first one is an intermixing factor (IM) at a given time t, which we define as

$$\text{IM} = 1 - \frac{\langle [\delta n_A(\mathbf{r}) - \delta n_C(\mathbf{r})]^2\rangle}{2\left[\langle \delta n_A^2(\mathbf{r})\rangle + \langle \delta n_C^2(\mathbf{r})\rangle\right]}, \tag{11}$$

where $\delta n_{A(C)} = n_{A(C)} - \langle n_{A(C)}\rangle$ and $\langle \ldots \rangle$ corresponds to the spatial average over position $\mathbf{r}$. In the case of complete intermixing or density overlap (with equal probability of A and C species occupying the same position), $\delta n_A = \delta n_C$ and thus $\text{IM} = 1$. In the other limit of no density overlap, i.e., $\int \delta n_A(\mathbf{r})\delta n_C(\mathbf{r}) d\mathbf{r} = 0$ and hence $\langle \delta n_A(\mathbf{r})\delta n_C(\mathbf{r})\rangle = 0$, we have $\text{IM} = 1/2$ without any intermixing. (Note that $\text{IM} = 0$ corresponds to the inverse atomic ordering between A and C with $\delta n_A = -\delta n_C$, such as the triangular A (or C) and honeycomb or inverse triangular C (or A) sublattice ordering [31], which can be viewed as the in-plane projection of metallic 1T phase of TMDs and is not studied here.)

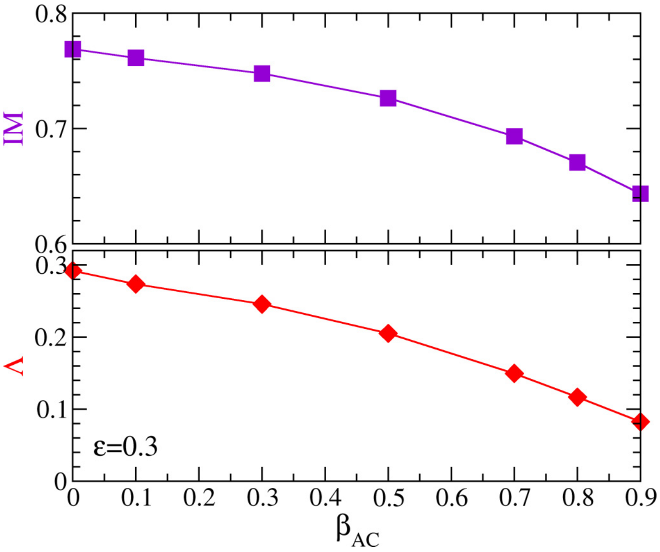

FIG. 3. The intermixing factor IM and the normalized overlap factor Λ as a function of β_{AC} at $\epsilon = 0.3$. The results have been averaged over 20 simulations (with error bars smaller than the size of symbols shown). Some of the corresponding atomic structures and correlation functions are given in Figs. 1 and 2, respectively.

Alternatively, an overlap factor Λ can be also used to quantify the intermixing, i.e.,

$$\Lambda = \frac{\langle \delta n_A(\mathbf{r})\delta n_C(\mathbf{r})\rangle^2}{\langle \delta n_A^2(\mathbf{r})\rangle\langle \delta n_C^2(\mathbf{r})\rangle}, \tag{12}$$

which is similar to the normalized overlap integral used in the study of mixing or demixing of binary species [43]. A full degree of intermixing (with complete density overlap $\delta n_A = \delta n_C$) leads to $\Lambda = 1$, while the complete lack of intermixing (with no overlap $\int \delta n_A(\mathbf{r})\delta n_C(\mathbf{r})d\mathbf{r} = 0$) yields $\Lambda = 0$. Generally this overlap factor Λ might give a better resolution for quantifying the degree of intermixing as compared to the intermixing factor IM described above (see, e.g., our calculation results in Figs. 3 and 4), due to a broader range of $0 \leqslant \Lambda \leqslant 1$ as compared to $1/2 \leqslant \mathrm{IM} \leqslant 1$. However, it should be noted that an ambiguity would occur when using Λ in the case of inverse sublattice ordering ($\delta n_A = -\delta n_C$), which also leads to $\Lambda = 1$. This ambiguity can be clarified through the combination with the IM calculation (which yields $\mathrm{IM} = 0$ for complete inverse ordering), and thus both Λ and IM are used in our quantitative analyses of intermixing.

Some results of IM and Λ for various values of β_{AC} at $\epsilon = 0.3$ (which correspond to the simulations conducted in Sec. III A and Figs. 1 and 2) are presented in Fig. 3, showing a small or moderate degree of intermixing. With the increase of β_{AC} (i.e., more energetic favoring of *A*-*C* heteroelemental coordination) as accompanied by the transition from *AB*-*CB* phase separation to atomic ordering, both values of IM and Λ decrease, indicating a lesser intermixing during the transition.

Importantly, our modeling also reveals an increased degree of intermixing or disordering (random alloying) between *A* and *C* species at higher growth temperature, consistent with that observed in recent experiments of TMD growth [6,13]. This is shown in the insets of Fig. 4, where values of IM and Λ become larger with the decrease of parameter ϵ, i.e., the increase of temperature. It can also be seen from the azimuthally averaged correlation function $C_{\text{A-C}}(r)$ plotted in Figs. 4(a) and 4(b), for locally phase-segregated (with $\beta_{AC} = 0.5$) and atomically ordered (with $\beta_{AC} = 0.9$) cases, respectively. The height of the first correlation maximum (peak) or minimum (valley) is reduced via lowering the value of ϵ, indicating less degree of *A*-*C* correlation at spacing $r = a_0$ of the *A* and/or *C* lattice and hence more disordering of the two species as a result of their mixing at higher temperature. The connection between *A*-*C* correlation and intermixing can be also obtained by rewriting Eq. (10) at a given time t as

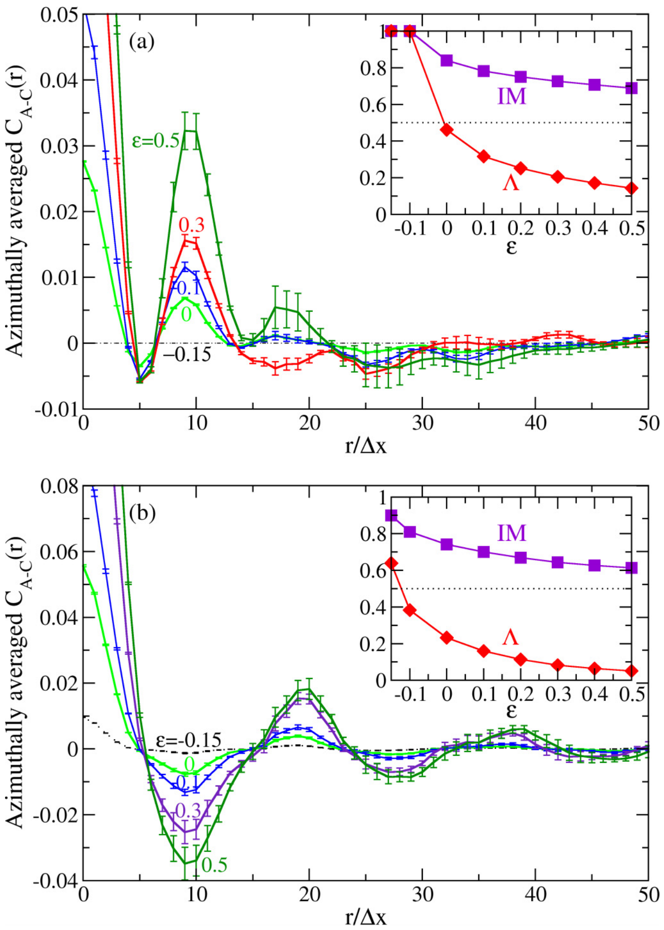

FIG. 4. Azimuthally averaged correlation function $C_{\text{A-C}}(r)$ for different values of ϵ at (a) $\beta_{AC} = 0.5$ and (b) $\beta_{AC} = 0.9$. The corresponding results for the degree of *A*-*C* intermixing are shown in the insets (where the error bars are smaller than the size of symbols). All the results have been averaged over 20 simulations.

$$C_{\text{A-C}}(\mathbf{r}) = \langle [\delta n_A(\mathbf{x}+\mathbf{r}) - \delta n_C(\mathbf{x}+\mathbf{r})][\delta n_A(\mathbf{x}) - \delta n_C(\mathbf{x})]\rangle, \tag{13}$$

such that $\mathrm{IM} = 1 - C_{\text{A-C}}(0)/2(\langle \delta n_A^2\rangle + \langle \delta n_C^2\rangle)$ from Eq. (11). Thus, a higher degree of intermixing at smaller ϵ (higher temperature) would lead to smaller $C_{\text{A-C}}(0)$, as verified in Fig. 4. In the limit of full intermixing with $\delta n_A \to \delta n_C$, *A* and *C* densities are then uncorrelated, i.e., $C_{\text{A-C}}(r) \to 0$ according to Eq. (13), as seen from the plots of $\epsilon = -0.15$ in Fig. 4.

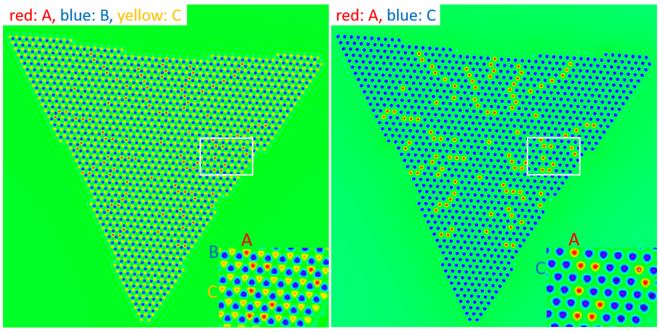

FIG. 5. The spatial distribution of A, B, and C species (left) and the corresponding A-C lattice structure (right) obtained from PFC simulation at $\epsilon = 0.3$, $\beta_{AC} = 0.9$, and $\psi_0 = -0.6$ with $n_{A0} = n_{B0} = -0.4532$ and $n_{C0} = -0.3128$. The white-boxed regions are enlarged as insets.

All the above results are for equal composition of A and C components with $n_{A0} = n_{C0}$. It is expected that at large enough composition disparity between the two species, a dispersed or random distribution of the minority species would occur. This binary disordered phase can be reproduced from our PFC simulations as well, with some sample results given in Fig. 5. Here we define the concentration of A component via $c_A = (1 + \psi_0)/2$ with

$$\psi_0 = \frac{\bar{\rho}_A - \bar{\rho}_C}{\bar{\rho}_A + \bar{\rho}_C} = \frac{n_{A0} - n_{C0}}{1 + n_{A0} + n_{C0}}, \tag{14}$$

where $\bar{\rho}_{A(C)}$ is the average of atomic number density $\rho_{A(C)}$ of A or C component. This is based on the definition of density variation fields $n_{A(C)} = (\rho_{A(C)} - \rho_{A(C)0})/\rho_0$ with $\rho_{A(C)0}$ the reference-state densities and $\rho_0 = \rho_{A0} + \rho_{C0}$, the choice of same reference state $\rho_{A0} = \rho_{C0}$, and $n_{A(C)0} = (\bar{\rho}_{A(C)} - \rho_{A(C)0})/\rho_0$. For the example of $\psi_0 = -0.6$ (with $c_A = 0.2$) at $\epsilon = 0.3$ and $\beta_{AC} = 0.9$, Fig. 5 shows an overall disordered A-C structure, while AB or CB still maintains its own binary honeycomb lattice (see the inset in the left panel of Fig. 5).

C. Heterostructures and multijunctions via lateral edge epitaxy

A starting point of our modeling of 2D heterostructural growth is the understanding of individual grain growth dynamics, based on some basic mechanisms and outcomes revealed in the study of binary AB grains [30,36]. As shown in Fig. 6, the grain shape can be controlled via chemical potentials μ_A and μ_B of A and B components in the PFC modeling, ranging from triangle, truncated triangle, to hexagon, and to more irregular shape with faceted surface consisting of terraces. The grain edges are along the zigzag direction of the honeycomb lattice as obtained from our simulations. When the conserved dynamics for density fields n_A and n_B are used and most of A-B model parameters remain unchanged, the variation of μ_A $(=\delta\mathcal{F}/\delta n_A)$ and μ_B $(=\delta\mathcal{F}/\delta n_B)$ can be effectively tuned by changing the values of average densities n_{A0} and n_{B0}, with $n_{A0} > n_{B0}$ (or $n_{A0} < n_{B0}$) corresponding to $\mu_A > \mu_B$ (or $\mu_A < \mu_B$), as confirmed in numerical simulations. In addition to grain shape control through the nucleated growth from an initial solid seed (leading to the results presented in Fig. 6), we are also able to change the shape of any as-grown grain via varying the relative average densities (i.e., relative chemical potentials) of the two components, so that the subsequent growth of new AB layers will transform the binary grain from its initial shape to a different one governed by the imposed relation of chemical potentials, while the AB sublattice ordering of the grain microstructure still maintains. Our simulation results are consistent with experiments [8,38,44] and first-principles DFT calculations [45] of 2D binary TMD materials, and have built the ground for the subsequent growth of lateral heterostructures, as detailed below.

Here we emulate the experimental growth process of lateral edge epitaxy, in which the specific configurations of heterostructures with domain composition segregation are grown sequentially via flux control. Some sample simulation results and the comparison to some experiments (e.g., Refs. [5,10]) are shown in Fig. 7. The model parameters are chosen to represent typical growth conditions, including $\epsilon = 0.3$ for low enough temperature to avoid substantial compositional intermixing across the heterointerface, and $\beta_{AC} = 0.9$ giving an intrinsic trend of atomic ordering (but not phase separation) in the bulk state of 2D ternary crystal as found in various ternary TMD monolayers [15–17]. The initial condition is a pregrown triangle-shaped AB grain (see, e.g., the first panel of Fig. 7 at $t = 0$), as prepared according to the binary grain growth mechanism illustrated in Fig. 6. In our PFC modeling, to facilitate the subsequent growth of CB compounds instead of AB we also initialize a homogeneous state of n_C with large enough average density n_{C0} throughout the system, while outside the AB crystalline grain setting an initial homogeneous n_A phase with small enough n_{A0} and thus low enough density of A-type precursors to prevent the formation of unwanted AB layers or interface alloying or intermixing. Specifically, to generate results given in the top panels of Fig. 7 we first set $n_{A0} = -0.55$ and $n_{B0} = -0.375$ outside

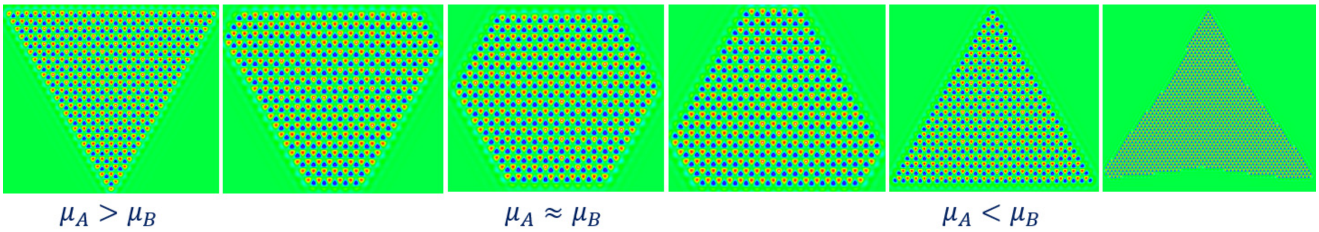

FIG. 6. Grain shape control in PFC simulations of AB binary honeycomb lattice, from triangle, truncated triangle, to hexagon shape, through the variation of chemical potentials μ_A and μ_B (via varying n_{A0} and n_{B0}) at $\epsilon_A = \epsilon_B = 0.3$. All the grains are of zigzag edges, with the density maxima of A and B components shown in red and blue, respectively.

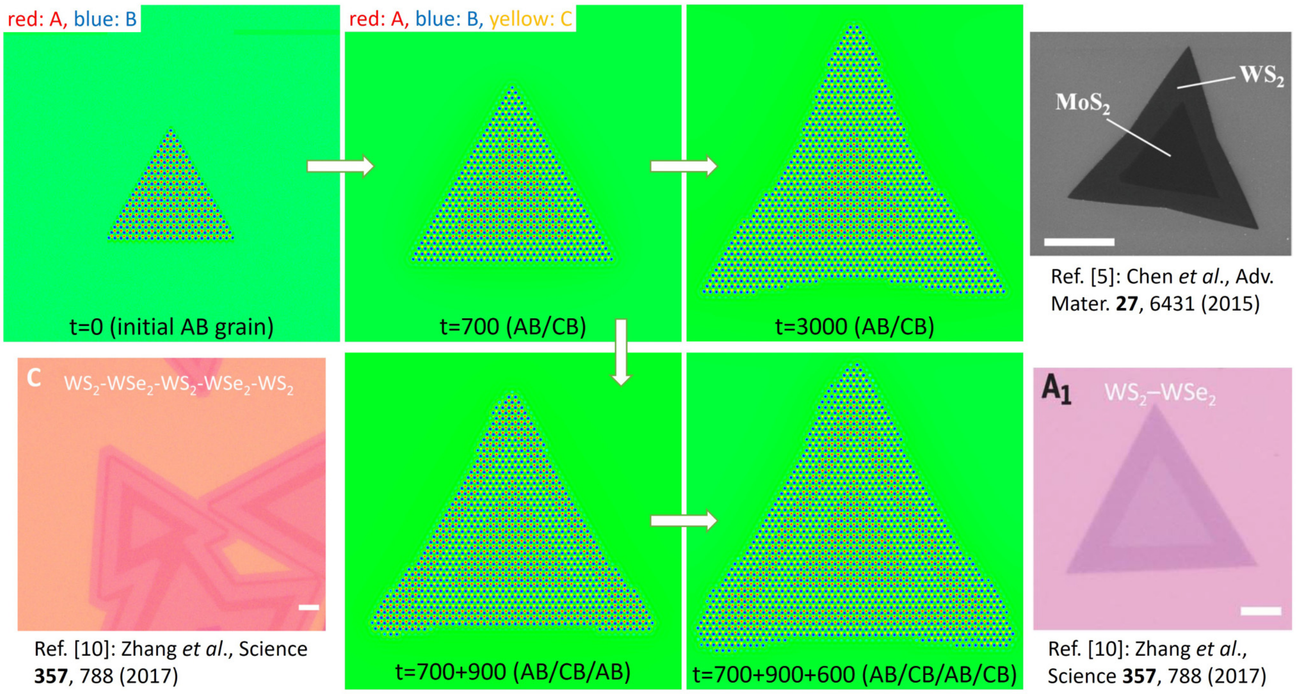

Ref. [5]: Chen *et al.*, Adv. Mater. **27**, 6431 (2015)

Ref. [10]: Zhang *et al.*, Science **357**, 788 (2017)

Ref. [10]: Zhang *et al.*, Science **357**, 788 (2017)

FIG. 7. PFC modeling for the growth of AB/CB lateral heterostructures and $AB/CB/AB$ and $AB/CB/AB/CB$ multijunctions or superlattices at $\epsilon = 0.3$ and $\beta_{AC} = 0.9$, with comparison to some recent experimental results (reprinted with permission from Ref. [5], copyright 2015 Wiley-VCH and from Ref. [10], copyright 2017 AAAS).

the initial AB grain, and $n_{C0} = -0.375$. The subsequent simulation shows the CB layer (of binary honeycomb lattice structure) grows epitaxially and laterally from the zigzag AB edge, forming an in-plane heterostructural grain with sharp and defect-free AB/CB heterointerface as well as faceted outer surface, consistent with the experimental findings of TMD lateral heterostructures in 2D triangle-shape crystals [1–8].

The subsequent growth of $AB/CB/AB$-type multijunctions requires a switch from the C-component rich to A-component dominated deposition flux, which can be effectively implemented by increasing the A-species density while reducing the C-species one (e.g., changing to $n_{A0} = n_{B0} = -0.375$ and $n_{C0} = -0.58$) outside the previously grown AB/CB crystallite. A step-by-step lateral epitaxial growth of the new AB layer from the outer zigzag edge of the 2D crystal then occurs, leading to the formation of planar multiple quantum wells (see the bottom panel of Fig. 7). A similar procedure can be followed to sequentially grow the in-plane superlattice consisting of alternative types of AB or CB blocks (each still forming its own binary honeycomb lattice). For the example of $AB/CB/AB/CB$ superlattice shown in Fig. 7, a depleted density of A component (with $n_{A0} = -0.59$ to avoid the nucleation of any new AB lattice) and high enough densities for C and B (with $n_{C0} = n_{B0} = -0.375$) are set in the initial homogeneous media outside the as-grown $AB/CB/AB$ grain, followed by the edge epitaxy of the new, outer CB layer. All these simulation outcomes well agree with the experimentally observed single-crystalline monolayers of coherently modulated lateral multiheterostructures or superlattices with straight and dislocation-free edges and heterojunctions (such as WS_2/WSe_2 [10,12] and $MoSe_2/WSe_2$ or MoS_2/WS_2 [11] monolayer superlattices or $WS_2/MoS_2/WS_2$ in-plane multijunctions [14]).

A potentially important but rarely explored configuration is a monolayer lateral heterostructure composed of distinct blocks of 2D ternary alloys, which could bring in an additional degree of freedom for heterostructural functionality control, in terms of the added flexibility of compositional variation and the composition-enabled tuning of electronic properties (e.g., band gap engineering) in each alloy block. Recently three-junction $MoS_{2(1-x)}Se_{2x}/WS_{2(1-x')}Se_{2x'}$ lateral alloy heterostructures were fabricated [11], where S and Se components in each individual block were observed to be completely miscible, with uniform alloying. Here we explore a different type of ternary-alloy-based lateral heterostructure or multijunction, which integrates ACB-type ternary alloy domains with atomic ordering that is achievable at low enough growth temperature, based on our related single-domain modeling in the above Secs. III A and III B as well as a recent experimental finding [17], which demonstrated the important effect of lattice atomic order on the electronic structure of 2D ternary TMD alloy $Re_{0.5}Nb_{0.5}S_2$.

Some sample configurations of such alloy-based lateral heterostructures predicted from PFC simulations are shown in Fig. 8. Similarly, we start from the same pregrown AB single crystal at $t = 0$ as in Fig. 7, which is surrounded by a homogeneous media, but with a larger flux and higher density of A component (same as that of component C, e.g., $n_{A0} = n_{C0} = -0.42$ and $n_{B0} = -0.375$) outside the initial AB grain. This leads to the formation of atomically ordered ACB ternary alloy from the zigzag lattice front, via the process of lateral edge epitaxy. The corresponding ternary lattice

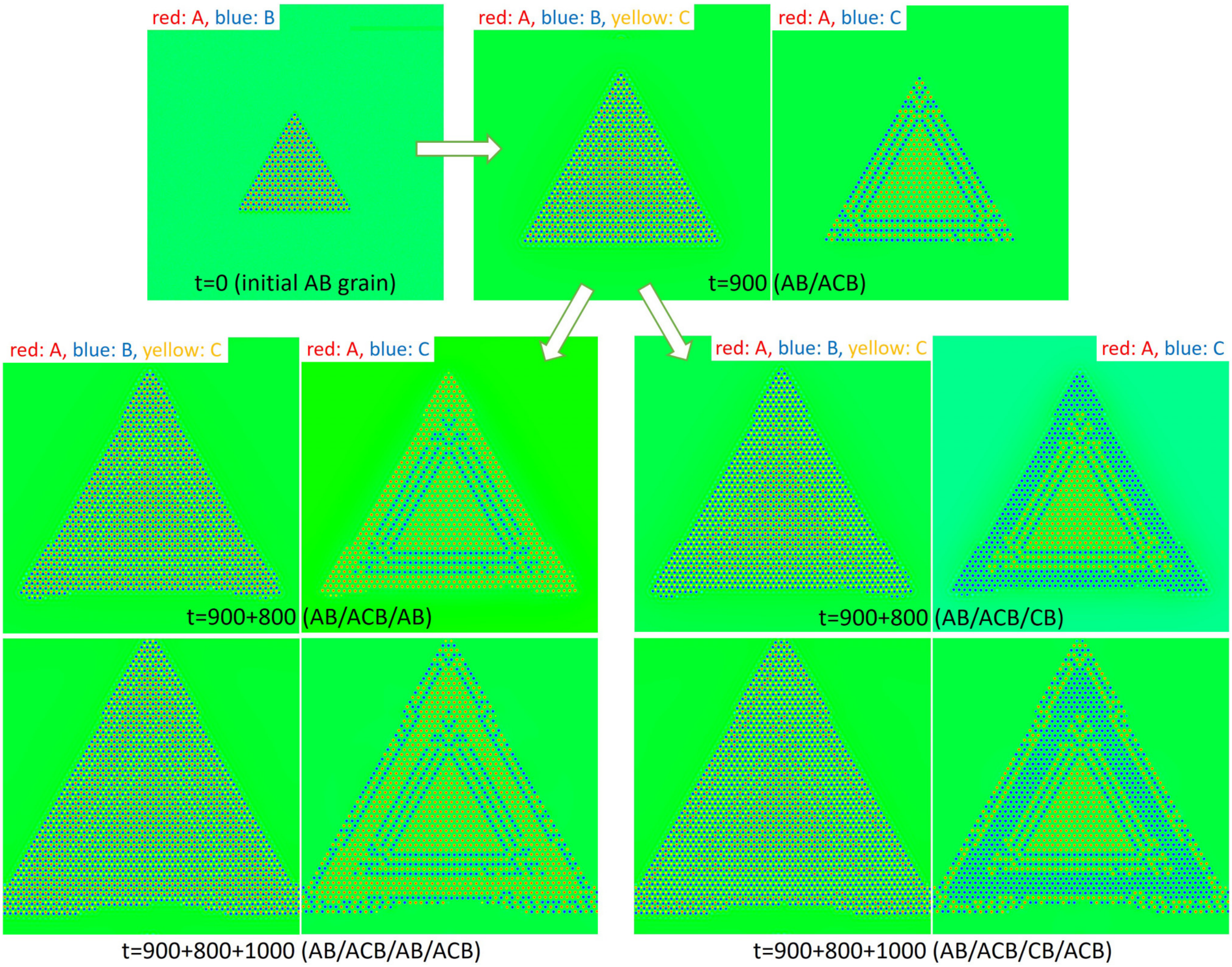

FIG. 8. The predicted growth procedure of lateral heterostructures and multijunctions consisting of *AB* and *CB* binary layers and *ACB* ternary layers with *A*-*C* atomic ordering. Both spatial configurations of *A*-*B*-*C* atomic densities and the corresponding *A*-*C* structures are shown. Results are obtained from PFC simulations at $\epsilon = 0.3$ and $\beta_{AC} = 0.9$.

structure is the same as that given in Fig. 1 at $\beta_{AC} = 0.9$ and $\epsilon = 0.3$, showing as *AB* and *CB* binary honeycomb rings plus the ordering between *A* and *C* components (see also the *A*-*C* density distribution in the top-right panel of Fig. 8). The resulting AB/ACB ordered heterostructure can maintain sharp heterointerface and faceted outer surface at low enough temperature.

A similar process of sequential growth via flux control can be adopted to produce a variety of lateral multijunctions or superlattices integrating domains of ternary 2D ordered alloys. The periodicity of these multiheterostructures and the types of their constituent blocks or units could be varied and controlled. Two such examples, $AB/ACB/AB/ACB$ superlattice and $AB/ACB/CB/ACB$ multijunctions, are demonstrated in Fig. 8 as obtained from our PFC simulations. For the first one, the above-mentioned AB/ACB growth procedure is continued but with the reduction of *C*-species density (to $n_{C0} = -0.58$ to turn off the *CB* growth) and the increase of *A* flux (with $n_{A0} = n_{B0} = -0.375$) outside the as-grown AB/ACB grain, yielding the edge epitaxy of the next *AB* layer and the in-plane $AB/ACB/AB$ heterostructure; switching back to the earlier flux condition (i.e., $n_{A0} = n_{C0} = -0.42$ and $n_{B0} = -0.375$) leads to the lateral coherent growth of the *ACB* ordered alloy again and hence an $AB/ACB/AB/ACB$ ordered-alloy-based superlattice. The same process of lateral epitaxy is followed in the second example to grow the in-plane $AB/ACB/CB/ACB$ multiheterostructure, with the only difference being in the mid step to form the *CB* (instead of *AB*) block from the as-grown *ACB* alloy edge, which then requires the setup of low enough *A*-precursor density ($n_{A0} = -0.58$) and high enough *C* and *B* densities (with $n_{C0} = n_{B0} = -0.375$) in the initial homogeneous phase surrounding the AB/ACB grain to enable the subsequent formation of $AB/ACB/CB$ multijunction.

An even richer variety of lateral multiheterostructures can be achieved by tuning the composition of different ternary alloy blocks as well as combining ordered and disordered alloy domains with varying types of heterointerfaces and junctions, which would result in functionally distinct but tunable heterostructural systems particularly in terms of optoelectronic or transport properties (with, e.g., various types of spatial modulation of band gaps and band alignments). All these in-plane structures can be prepared via the similar edge-epitaxial growth procedure described above with the control of deposition fluxes and temperature, which would significantly expand the range of potential 2D material systems or configurations with controllable functionality.

IV. CONCLUSIONS

We have developed a ternary phase field crystal model to study the growth and evolution processes of 2D crystals and in-plane lateral heterostructures of ternary hexagonal materials that are spatially and compositionally modulated. In this *A*-*B*-*C* ternary alloy with each of the *AB* and *CB* compounds forming a binary honeycomb structure, a transition from the phase-separated state between *AB* and *CB* domains, to an *A*-*C* atomically ordered phase with geometric frustration as found in a recent experiment of 2D ternary TMD alloy, can be achieved by controlling the degree of energetic preference of heteroelemental neighboring between *A* and *C* components. The results are quantified through the calculations of spatial correlation functions, and also of an intermixing factor and an overlap factor for identifying the degree of compositional intermixing or disordering, which is shown to increase at higher growth temperature, consistent with experimental observations.

These findings for 2D single-crystalline ternary grains are used as the basics to probe the growth of a variety of in-plane heterostructures, multijunctions, and superlattices. Sample results of AB/CB-, $AB/CB/AB$-, and $AB/CB/AB/CB$-type multiheterostructures are produced in our PFC simulations through a sequential growth process of lateral edge epitaxy, well agreeing with recent experimental outcomes of 2D TMD/TMD lateral heterostructures and superlattices. Importantly, our findings are extended to predict a new type of alloy-based in-plane heterostructures integrating blocks of *ACB*-type ternary alloy with atomic ordering, such as AB/ACB-type ordered-alloy heterostructure, $AB/ACB/AB/ACB$ superlattice, and $AB/ACB/CB/ACB$ multijunctions. This can be achieved through the control of the constituent densities and fluxes at each growth stage and the growth temperature, giving a viable way for exploring a wider variety of 2D heterostructural material systems.

ACKNOWLEDGMENTS

This work was supported by the National Science Foundation under Grant No. DMR-2006446.

[1] C. Huang, S. Wu, A. M. Sanchez, J. J. P. Peters, R. Beanland, J. S. Ross, P. Rivera, W. Yao, D. H. Cobden, and X. Xu, Lateral heterojunctions within monolayer $MoSe_2$ - WSe_2 semiconductors, Nature Mater. **13**, 1096 (2014).

[2] Y. Gong, J. Lin, X. Wang, G. Shi, S. Lei, Z. Lin, X. Zou, G. Ye, R. Vajtai, B. I. Yakobson, H. Terrones, M. Terrones, B. K. Tay, J. Lou, S. T. Pantelides, Z. Liu, W. Zhou, and P. M. Ajaya, Vertical and in-plane heterostructures from WS_2/MoS_2 monolayers, Nature Mater. **13**, 1135 (2014).

[3] X. Duan, C. Wang, J. C. Shaw, R. Cheng, Y. Chen, H. Li, X. Wu, Y. Tang, Q. Zhang, A. Pan, J. Jiang, R. Yu, Y. Huang, and X. Duan, Lateral epitaxial growth of two-dimensional layered semiconductor heterojunctions, Nature Nanotechnol. **9**, 1024 (2014).

[4] M.-Y. Li, Y. Shi, C.-C. Cheng, L.-S. Lu, Y.-C. Lin, H.-L. Tang, M.-L. Tsai, C.-W. Chu, K.-H. Wei, J.-H. He, W.-H. Chang, K. Suenaga, and L.-J. Li, Epitaxial growth of a monolayer WSe_2 - MoS_2 lateral p-n junction with an atomically sharp interface, Science **349**, 524 (2015).

[5] K. Chen, X. Wan, W. Xie, J. Wen, Z. Kang, X. Zeng, H. Chen, and J. Xu, Lateral built-in potential of monolayer MoS_2 - WS_2 in-plane heterostructures by a shortcut growth strategy, Adv. Mater. **27**, 6431 (2015).

[6] K. Bogaert, S. Liu, J. Chesin, D. Titow, S. Gradeccak, and S. Garaj, Diffusion-mediated synthesis of MoS_2/WS_2 lateral heterostructures, Nano Lett. **16**, 5129 (2016).

[7] Y. Zhang, L. Yin, J. Chu, T. A. Shifa, J. Xia, F. Wang, Y. Wen, X. Zhan, Z. Wang, and J. He, Edge-epitaxial growth of 2D NbS_2 - WS_2 lateral metal-semiconductor heterostructures, Adv. Mater. **30**, 1803665 (2018).

[8] Y. Zhang, Y. Yao, M. G. Sendeku, L. Yin, X. Zhan, F. Wang, Z. Wang, and J. He, Recent progress in CVD growth of 2D transition metal dichalcogenides and related heterostructures, Adv. Mater. **31**, 1901694 (2019).

[9] Q. Li, M. Liu, Y. Zhang, and Z. Liu, Hexagonal boron nitride-graphene heterostructures: Synthesis and interfacial properties, Small **12**, 32 (2016).

[10] Z. Zhang, P. Chen, X. Duan, K. Zang, J. Luo, and X. Duan, Robust epitaxial growth of two-dimensional heterostructures, multiheterostructures, and superlattices, Science **357**, 788 (2017).

[11] P. K. Sahoo, S. Memaran, Y. Xin, L. Balicas, and H. R. Gutiérrez, One-pot growth of two-dimensional lateral heterostructures via sequential edge-epitaxy, Nature (London) **553**, 63 (2018).

[12] S. Xie Jr., L. Tu, Y. Han, L. Huang, K. Kang, K. U. Lao, P. Poddar, C. Park, D. A. Muller, R. A. DiStasio, and J. Park, Coherent, atomically thin transition-metal dichalcogenide superlattices with engineered strain, Science **359**, 1131 (2018).

[13] K.-C. Chiu, K.-H. Huang, C.-A. Chen, Y.-Y. Lai, X.-Q. Zhang, E.-C. Lin, M.-H. Chuang, J.-M. Wu, and Y.-H. Lee, Synthesis of in-plane artificial lattices of monolayer multijunctions, Adv. Mater. **30**, 1704796 (2018).

[14] Y. Kobayashi, S. Yoshida, M. Maruyama, H. Mogi, K. Murase, Y. Maniwa, O. Takeuchi, S. Okada, H. Shigekawa, and Y. Miyata, Continuous heteroepitaxy of two-dimensional heterostructures based on layered chalcogenides, ACS Nano **13**, 7527 (2019).

[15] L.-Y. Gan, Q. Zhang, Y.-J. Zhao, Y. Cheng, and U. Schwingenschlögl, Order-disorder phase transitions in the two-dimensional semiconducting transition metal dichalcogenide alloys $Mo_{1-x}W_xX_2$ ($X = S$, Se, and Te), Sci. Rep. **4**, 6691 (2014).

[16] J.-H. Yang and B. I. Yakobson, Unusual negative formation enthalpies and atomic ordering in isovalent alloys of transition metal dichalcogenide monolayers, Chem. Mater. **30**, 1547 (2018).

[17] A. Azizi, M. Dogan, J. D. Cain, R. Eskandari, X. Yu, E. C. Glazer, M. L. Cohen, and A. Zettl, Frustration and Atomic Ordering in a Monolayer Semiconductor Alloy, Phys. Rev. Lett. **124**, 096101 (2020).

[18] Y. Chen, J. Xi, D. O. Dumcenco, Z. Liu, K. Suenaga, D. Wang, Z. Shuai, Y.-S. Huang, and L. Xie, Tunable band gap photoluminescence from atomically thin transition-metal dichalcogenide alloys, ACS Nano **7**, 4610 (2013).

[19] K. R. Elder, N. Provatas, J. Berry, P. Stefanovic, and M. Grant, Phase field crystal modeling and classical density functional theory of freezing, Phys. Rev. B **75**, 064107 (2007).

[20] Z.-F. Huang and K. R. Elder, Mesoscopic and Microscopic Modeling of Island Formation in Strained Film Epitaxy, Phys. Rev. Lett. **101**, 158701 (2008).

[21] M. Greenwood, N. Provatas, and J. Rottler, Free Energy Functionals for Efficient Phase Field Crystal Modeling of Structural Phase Transformations, Phys. Rev. Lett. **105**, 045702 (2010).

[22] S. K. Mkhonta, K. R. Elder, and Z.-F. Huang, Exploring the Complex World of Two-Dimensional Ordering with Three Modes, Phys. Rev. Lett. **111**, 035501 (2013).

[23] H. Emmerich, H. Löwen, R. Wittkowski, T. Gruhn, G. I. Tóth, G. Tegze, and L. Gránásy, Phase-field-crystal models for condensed matter dynamics on atomic length and diffusive time scales: An overview, Adv. Phys. **61**, 665 (2012).

[24] N. Ofori-Opoku, V. Fallah, M. Greenwood, S. Esmaeili, and N. Provatas, Multicomponent phase-field crystal model for structural transformations in metal alloys, Phys. Rev. B **87**, 134105 (2013).

[25] E. Alster, K. R. Elder, J. J. Hoyt, and P. W. Voorhees, Phase-field-crystal model for ordered crystals, Phys. Rev. E **95**, 022105 (2017).

[26] E. Alster, D. Montiel, K. Thornton, and P. W. Voorhees, Simulating complex crystal structures using the phase-field crystal model, Phys. Rev. Materials **1**, 060801(R) (2017).

[27] M. Salvalaglio, A. Voigt, Z.-F. Huang, and K. R. Elder, Mesoscale Defect Motion in Binary Systems: Effects of Compositional Strain and Cottrell Atmospheres, Phys. Rev. Lett. **126**, 185502 (2021).

[28] P. Hirvonen, M. M. Ervasti, Z. Fan, M. Jalalvand, M. Seymour, S. M. Vaez Allaei, N. Provatas, A. Harju, K. R. Elder, and T. Ala-Nissila, Multiscale modeling of polycrystalline graphene: A comparison of structure and defect energies of realistic samples from phase field crystal models, Phys. Rev. B **94**, 035414 (2016).

[29] M. Seymour and N. Provatas, Structural phase field crystal approach for modeling graphene and other two-dimensional structures, Phys. Rev. B **93**, 035447 (2016).

[30] D. Taha, S. K. Mkhonta, K. R. Elder, and Z.-F. Huang, Grain Boundary Structures and Collective Dynamics of Inversion Domains in Binary Two-Dimensional Materials, Phys. Rev. Lett. **118**, 255501 (2017).

[31] D. Taha, S. R. Dlamini, S. K. Mkhonta, K. R. Elder, and Z.-F. Huang, Phase ordering, transformation, and grain growth of two-dimensional binary colloidal crystals: A phase field crystal modeling, Phys. Rev. Mater. **3**, 095603 (2019).

[32] W. Zhou, J. Wang, B. Lin, Z. Wang, J. Li, and Z.-F. Huang, Yielding and jerky plasticity of tilt grain boundaries in high-temperature graphene, Carbon **153**, 242 (2019).

[33] P. Hirvonen, V. Heinonen, H. Dong, Z. Fan, K. R. Elder, and T. Ala-Nissila, Phase-field crystal model for heterostructures, Phys. Rev. B **100**, 165412 (2019).

[34] K. R. Elder, C. V. Achim, V. Heinonen, E. Granato, S. C. Ying, and T. Ala-Nissila, Modeling buckling and topological defects in stacked two-dimensional layers of graphene and hexagonal boron nitride, Phys. Rev. Mater. **5**, 034004 (2021).

[35] H. Dong, P. Hirvonen, Z. Fan, and T. Ala-Nissila, Heat transport in pristine and polycrystalline single-layer hexagonal boron nitride, Phys. Chem. Chem. Phys. **20**, 24602 (2018).

[36] B. Waters and Z.-F. Huang, Grain rotation and coupled grain boundary motion in two-dimensional binary hexagonal materials, Acta Mater. **225**, 117583 (2022).

[37] J. Zhou, J. Lin, X. Huang, Y. Zhou, Y. Chen, J. Xia, H. Wang, Y. Xie, H. Yu, J. Lei, D. Wu, F. Liu, Q. Fu, Q. Zeng, C.-H. Hsu, C. Yang, L. Lu, T. Yu, Z. Shen, H. Lin, et al., A library of atomically thin metal chalcogenides, Nature (London) **556**, 355 (2018).

[38] S. G. Sorensen, H. G. Füchtbauer, A. K. Tuxen, A. S. Walton, and J. V. Lauritsen, Structure and electronic properties of *in situ* synthesized single-layer MoS_2 on a gold surface, ACS Nano **8**, 6788 (2014).

[39] X. Zou, Y. Liu, and B. I. Yakobson, Predicting dislocations and grain boundaries in two-dimensional metal-disulfides from the first principles, Nano Lett. **13**, 253 (2013).

[40] W. Zhou, X. Zou, S. Najmaei, Z. Liu, Y. Shi, J. Kong, J. Lou, P. M. Ajayan, B. I. Yakobson, and J.-C. Idrobo, Intrinsic structural defects in monolayer molybdenum disulfide, Nano Lett. **13**, 2615 (2013).

[41] A. N. Enyashin, M. Bar-Sadan, L. Houben, and G. Seifert, Line defects in molybdenum disulfide layers, J. Phys. Chem. C **117**, 10842 (2013).

[42] H. Liu, L. Jiao, F. Yang, Y. Cai, X. Wu, W. Ho, C. Gao, J. Jia, N. Wang, H. Fan, W. Yao, and M. Xie, Dense Network of One-Dimensional Midgap Metallic Modes in Monolayer $MoSe_2$ and their spatial undulations, Phys. Rev. Lett. **113**, 066105 (2014).

[43] P. Jain and M. Boninsegni, Quantum demixing in binary mixtures of dipolar bosons, Phys. Rev. A **83**, 023602 (2011).

[44] S. Wang, Y. Rong, M. P. Ye Fan, H. Bhaskaran, K. He, and J. H. Warner, Shape evolution of monolayer MoS_2 crystals grown by chemical vapor deposition, Chem. Mater. **26**, 6371 (2014).

[45] H. Schweiger, P. Raybaud, G. Kresse, and H. Toulhoat, Shape and edge sites modifications of MoS_2 catalytic nanoparticles induced by working conditions: A theoretical study, J. Catal. **207**, 76 (2002).